

© 2009 Yupeng Qiu

ULTRASONIC VISCOELASTICITY IMAGING OF
NONPALPABLE BREAST LESIONS

BY

YUPENG QIU

THESIS

Submitted in partial fulfillment of the requirements
for the degree of Master of Science in Bioengineering
in the Graduate College of the
University of Illinois at Urbana-Champaign, 2009

Urbana, Illinois

Advisor:

Professor Michael F. Insana

Abstract

The prognosis of breast cancer patients improves with early and accurate diagnosis. The quality of the strain image produced by displacement estimation algorithms are heavily influenced by the RF echo data recorded by different ultrasound systems. A small clinical study was conducted with 21 women having a single nonpalpable breast lesion, each detected mammographically with later pathology confirmation. Elasticity images were acquired on each patient to test for the ability to differentiating malignant and benign lesions. The mechanical relaxation time T_1 images showed a tissue-specific T_1 contrast that is negative for all 11 malignant lesions and positive for all 10 benign lesions. Strain images were estimated using a regularized multi-scale optical flow (ROF) algorithm. Adjustments to the input parameters to the ROF and their subsequent effects on T_1 estimation and computation time are shown to have a strong effect on diagnostic performance.

To My Parents and Grandparents.

Acknowledgments

This work is supported by the NCI under award No. CA082497 and by the Beckman Institute for Advanced Science and Technology at the University of Illinois.

Table of Contents

List of Tables	vi
List of Figures	vii
List of Abbreviations	viii
List of Symbols	ix
Chapter 1 Introduction	1
Chapter 2 Phantom Imaging	3
2.1 Processing Algorithms	3
2.1.1 Companding Algorithm	3
2.1.2 Optical Flow Algorithm	6
2.2 Making the Phantom	8
2.3 Imaging Techniques	9
2.4 Processing the RF Data	10
2.4.1 RF Data From 2 Systems	10
2.4.2 Processing of 4 Frames per Second RF Data	10
2.4.3 Processing of 17 Frames per Second RF Data	12
2.4.4 Viscoelasticity Imaging	16
2.5 Conclusions	18
Chapter 3 Patient Imaging	19
3.1 Methods	19
3.1.1 Patient Selection	19
3.1.2 Lesion Diagnoses	20
3.1.3 Imaging Techniques	21
3.1.4 Curve Fitting	21
3.1.5 Pixel Selection and Averaging	22
3.1.6 Parametric Contrast	23
3.1.7 The Three Adjustable ROF Parameters	24
3.2 Results	26
3.2.1 Statistical Analysis	26
3.2.2 Contrast Histograms and Scatter Plot	27
3.2.3 Color Imaging	27
3.3 Conclusions	28
Chapter 4 Conclusions	31
Appendix A SonixRP Adjustments	33
References	35

List of Tables

3.1	T_1 Computation Time for Different Number of Scale Levels	25
3.2	T_1 Computation Time for Different Search Window Sizes	26
3.3	Student's T-test Results from Viscoelastic Parameters	26

List of Figures

2.1	Diagram of a Data Kernel Search	4
2.2	Global and Local Companding Diagrams	5
2.3	ROF Displacement Estimation	8
2.4	Schematic of the Mold Used for Creating Elasticity Imaging Gel Phantoms	9
2.5	Antares and SonixRP B-mode Images	11
2.6	Antares and SonixRP before Adjustments Strain Images	11
2.7	Antares and SonixRP after Adjustments Strain Images	12
2.8	Antares 17 FPS Strain Image before Adjustments	13
2.9	Displacement and Strain Plots for a Single Scanline with Quantization Error in the Image Matrix	14
2.10	Companded Displacement and Strain Plots for a Single Scanline with Corrections for Companding in the Image Matrix	14
2.11	Companded-Only Strain Image before and after Corrections	14
2.12	ROF Displacement Plots for a Single Scanline with Errors in the Image Matrix	15
2.13	ROF Displacement and Strain Plots for a Single Scanline with Corrections for ROF in the Image Matrix	16
2.14	Antares 17 FPS Strain Image after Adjustments	16
2.15	ROF Displacement and Strain Plots for a Single Scanline in the Image Matrix	17
2.16	SonixRP 17 FPS Strain Image after Adjustments	17
3.1	Multicompression RF Echo Acquisition, Strain Image Formation, and VE Parameter Estimation for a Patient with a Nonpalpable Fibroadenoma	22
3.2	Examples of Malignant and Benign Viscoelastic Strain Curves	23
3.3	Example of Pixel Selection for Statistical Analysis	23
3.4	Strain Images with Different α	24
3.5	T_1 Estimates from the Lesion and Background Tissues Collected at Different α Values	25
3.6	Average Lesion Parameters	26
3.7	Patient Average VE Contrast Values	28
3.8	Scatter Plot of Patient Contrast Values for Two Parameters, ϵ_0 and T_1	28
3.9	Sonograms with T_1 Parametric Color Overlays	29
A.1	Diagram for 192 Scanlines Center Virtual Element Assignment	33

List of Abbreviations

VE	Viscoelastic.
BI-RADS	Breast Imaging Reporting and Data System.
IDC	Infiltrating Ductal Carcinoma.
ILC	Infiltrating Lobular Carcinoma.
FA	Fibroadenoma.
FC	Fibrocystic Change.
UCD	University of California at Davis.
UIUC	University of Illinois at Urbana-Champaign.
URI	Ultrasound Research Interface.
RF	Radio-Frequency.
FPS	Frames per Second.
SBR	Scarff-Bloom-Richardson.
IRB	Institutional Review Board

List of Symbols

T_1	The Relaxation Time in Seconds of the Exponential Creep Curve.
ϵ_0	The Instantaneous Elastic Strain.
ϵ_1	The Amplitude of the Exponential Creep Curve.

Chapter 1

Introduction

Breast cancer is the fifth most common cause of cancer death worldwide, and the most frequently diagnosed cancer in women [1]. In the US during 2007, it was expected that approximately 178,480 women would develop invasive breast cancer and an estimated 40,910 patients will die from this disease. The combined efforts of early detection and improved treatment have steadily decreased the death rate in women from breast cancer since 1990. The earliest cancer signs are detectable by medical imaging often before symptoms appear. Diagnosis is currently based on information obtained from the clinical examination, anatomical imaging, and biopsy. Although histopathology is the gold standard for diagnosis, the biopsy procedure is invasive, expensive and carries some risk. Therefore, additional noninvasive diagnostic imaging method to increase specificity and reduce the need for biopsy would be beneficial.

Recent discoveries in molecular biology have triggered interest in developing new and potentially more specific imaging methods for breast cancer diagnosis [2]. These include techniques for (a) direct imaging of signaling molecules and/or receptors mediating malignant progression, and (b) indirect imaging of intrinsic tissue properties (e.g., biochemical, mechanical) that describe the tumor microenvironment controlling signaling pathways. We use the latter method to detect local changes in soft tissue. The alteration in elasticity properties is in part a result of inflammation that usually occurs during the early stages of disease development. The extracellular matrix (ECM) of breast stroma, which provides the solid consistency of parenchymal tissues, plays an active role in cancerous tumor growth [3]. Hence, breast stroma is a potentially valuable source of endogenous disease-specific contrast.

The term "elasticity imaging" refers to any application of imaging technologies to the spatiotemporal description of the mechanical properties of a medium [4]. Medical elasticity imaging is broadly categorized as dynamic or quasi-static, where in both cases a small applied force creates tissue deformations that may be tracked by ultrasonic, magnetic resonance, or optical imaging technologies. Dynamic methods for imaging viscoelastic breast features stimulate tissues with harmonic [5, 6] or impulse [7, 8] forces, typically in the micro-to-milliNewton (μN - mN) amplitude range and at frequencies above 50 Hz.

We employ quasi-static ultrasonic methods for viscoelastic breast imaging. Echo movements are tracked

as an ultrasonic probe is gently pressed into the skin surface. Step-force amplitudes of 3-6 N¹ are applied suddenly and handheld constant for 10-20 s while ultrasonic echo data are acquired to track movements in a series of strain images. Such methods are quasi-static because the frequency range for this force stimulus is less than about 1 Hz [9]. The slow movement of tissue under a load - called viscous creep - is characteristic of the viscoelastic (VE) properties of tissues. VE properties are found by analyzing a time series of elastic strain images. Because creep responses to mechanical forces vary in soft tissues and other hydropolymers with the frequency of the force stimulus, dynamic and quasi-static methods are thought to provide independent information. It is not yet known which part of the force bandwidth has the most diagnostic information.

Recent studies [10, 11, 12, 13] suggest that elastic strain images of breast tissue can be effective at discriminating focal benign and malignant tumors. Thomas et al. [11] showed that strain and strain-rate images were most effective when diagnosing BI-RADS (Breast Imaging-Reporting and Data System) 3 lesions with lipomatous involution and somewhat less effective with BI-RADS 4 or 5 lesions. A sensitive diagnostic feature was the ratio of lesion size visualized in strain images versus that in spatially registered sonograms, suggesting that many of the malignancies studied had a palpable degree of desmoplasia thereby appearing larger on strain images than sonograms. Zhi et al [12] also showed that strain imaging was effective at malignant-benign discrimination for late-stage tumors. However, with strain images, early stage (I & II) infiltrating ductal carcinomas (IDCs) were misdiagnosed presumably because of the lack of desmoplasia. Although lesion palpability and size were not selection criteria for patients in these prior studies, more than half of the lesions were identified as palpable and the maximum tumor diameter ranged from 0.3 cm to 10 cm. The purpose of our preliminary patient study was to determine whether viscoelastic features improved benign vs. malignant differentiation for nonpalpable breast lesions discovered on mammographic scanners.

One of the most important feature that we look for is image contrast. In this case, the image contrasts resulting from any of the viscoelastic parameters are based on estimations from algorithms that track the displacements of RF echo signals recorded by ultrasound systems. The ability of the ultrasound systems to record small movements and the ability of the algorithms to estimate the necessary displacement maps for the estimation of strain images are important. In the next section, we conducted a series of testings with a tissue-mimicking phantom and two ultrasound systems with different hardwares (resulting in slightly different recorded RF echo signals) and compare the strain images obtained from the algorithms.

¹For comparison, mammographic compressional forces are 100-200 N

Chapter 2

Phantom Imaging

2.1 Processing Algorithms

2.1.1 Companding Algorithm

The companding program by Chaturvedi et. al [14] is normally used for the processing of RF data acquired from the compression of tissue-mimicking phantoms. Companding is a process in which a before-compression RF image is conditioned such that the image will match the post-compressed RF data as much as possible (the same can be applied vice-versa). The algorithm is split into two parts: global companding, where a coarse grid is used to roughly stretch the post-compressed image frame; and local companding, where the fine tuning between the two images happen. Both processes use the same Sum-Absolute-Difference (SAD) algorithm [15, 16] to determine the new pixel position.

The theoretical of the algorithms and their applications in the Matlab code are explained below:

Global Companding

In global companding, the image grid is separated into a number of non-overlapping blocks which we call data kernels. We then select a search region in the following image and try to find the best match for each data kernel. If we let the data kernel size be $L \times M$, the search region size be $P \times Q$, the pixel positions be i, j , and the uncompressed and compressed frames be U and C respectively, we can find the minimum SAD coefficient, $\delta_{i,j}$ by minimizing the following SAD equation:

$$\delta_{i,j} = \sum_{l=1}^L \sum_{m=1}^M |C_{l,m} - U_{l+i,m+j}| \quad (2.1)$$

Figure 2.1 is a schematic of this kernel search.

In actual programming code, global companding is done by a C-executable code to increase the processing speed. Because the kernels are non-overlapping, the program simply divides the input data matrix into blocks as shown in Figure 2.2a. The size of the kernels in the axial direction is determined by the user (set to 120

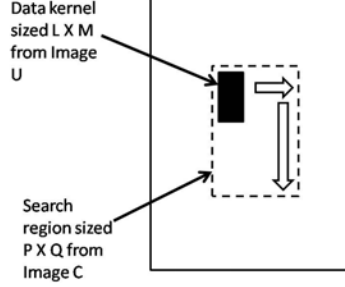


Figure 2.1: Diagram of a Data Kernel Search. Assuming that U and C are of equal sized matrices, take a data kernel sized $L \times M$ from U and find the most probably location for it in a search region sized $P \times Q$ from C , the deciding factor is the minimum error as determined by equation 2.1.

rows) assuming that the axial sampling frequency is always 40 MHz while the number of kernels in the lateral direction is set to 8, therefore the lateral kernel size is determined by the lateral image size, this is to ensure that the data kernels are not too large if the lateral resolution is low.

The program outputs a number of new center coordinates and their displacements for each data kernel. Matlab then takes in these center coordinates and displacements to find the original center coordinates, then performs linear regression to find the strain and shift estimations in the axial and lateral directions. Finally, a 2D interpolation is performed using these estimations to stretch the data kernels, Thus companding image U to match image C .

Local Companding

Local companding is very similar to global companding except in 2 aspects: the data kernels now overlap and the size of the data kernels is smaller.

In actual programming code, local companding is done by a C-executable code to increase the processing speed. The data kernel size is determined by the user (set to 80 rows by 8 columns). The overlapping procedure is done by moving the data kernels down (axially) 10 rows at a time and moving the data kernels left/right (laterally) 2 columns at a time as seen in Figure 2.2b. The maximum search window size is also pre-determined by the user (set to 160 rows by 24 columns).

The search direction is as follows:

1. For a certain data kernel located on a certain row, m , the program searches down the center column of the overall image matrix in the previously defined search region size to locate a initial pixel position (i_{min}, j_{min}) . The SAD algorithm is used to match the data kernels each time and return the index value matching the minimum SAD coefficient.

2. The search then goes 2 ways, from the center column to the left side of the image matrix and from the center column to the right side of the image matrix, these two processes are similar except for the countdown of column numbers, therefore only the left side search process will be described in the next step.
3. The search window region is also flexible now, depending on the minimum pixel position values obtained previously, with the smallest possible search window region being 3×3 pixels. As the search progresses towards the bottom of the image, the search window size also returns to the maximum possible search region in order to account for more pixel displacements towards the bottom of the image matrix. The SAD algorithm is again used to find the index values matching the minimum SAD coefficients for every other column, n , on a specific row, m .
4. The program then shifts down 10 rows and the process begins again.

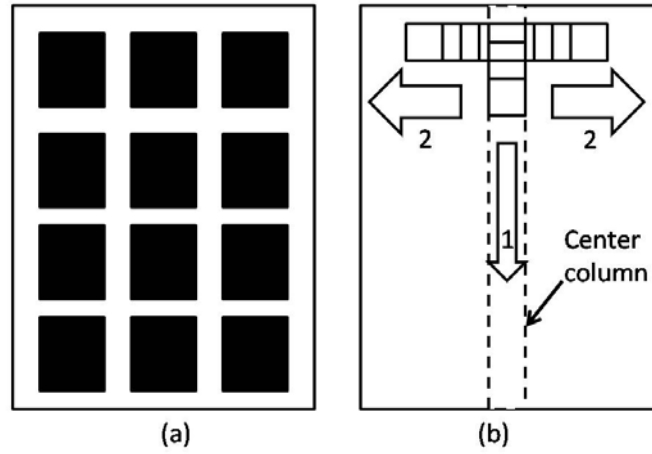


Figure 2.2: Global and Local Companding Diagrams. (a)Global companding diagram. The image matrix is divided into non-overlapping data kernels of a specific size depending on the size of the image matrix ; (b)Local companding diagram. The data kernels overlap each other. The number 1 depicts step 1 in the local companding search process, the number 2 depicts step 2 in the local companding search process. Data kernels skip every 10 rows when it is moving down (axial direction) and they skip every 2 columns when it is moving left/right (lateral direction)

After this is done for the entire image matrix, we obtain an axial and a lateral index map. Since we skipped the data for every 10 rows and every 2 columns, we need to define the index values for every skipped pixel. Assuming that displacement is linear in a small distance, we use a simple linear interpolation to find the index values.

Finally, local companding conditions the data matrix via nearest-neighbor 2-D interpolation in order to locally deform image U to more closely approximate image C for the eventual correlation process.

Companded Displacement

The C-programming code for local companding results in a conditioned image set as well as the the new pixel position values. To find the displacement along the beam axis, we simply need to define the original pixel position values along the beam axis and then find the difference. This is what is known as the companded difference in the Matlab program. Since we know that each segment of displacement should be linear, we can apply a simple smoothing filter to minimize noise. The size of the smoothing window is set to 16 pixels.

Correlated Displacement

The companding program can only condition image C to approximate image U, therefore, we use the correlation algorithm to find the remaining displacements. The correlation window size is set by the user (default at 256 samples/rows). At each iteration (sample length is 256 rows) in the Matlab code, all columns of the image matrix are produced. Given 2 complex signals $s1$ and $s2$, the complex cross correlation equation $corr_{s1,s2}(x)$ is defined as

$$corr_{s1,s2}(x) = s1(x) \times s2^*(x) = \int_{-\infty}^{\infty} s1(x)s2^*(u-x)du \quad (2.2)$$

In Matlab, the sequence is carried out using the Fast Fourier Transform (FFT) and Inverse Fast Fourier Transform (IFFT) functions with the previously described sample size.

The same smoothing filter (window length = 16 pixels) is also applied to the correlated displacement map.

Strain

The companded displacement map and the correlated displacement map are added to produce the total displacement estimated between adjacent RF data frames. The strain is found by taking the derivative of the total displacement map.

2.1.2 Optical Flow Algorithm

The regularized optical flow algorithm (ROF) [17] estimates the displacement fields between adjacent frames recorded during compression, and the derivative of the sum displacement field is used to find the strain image. The general equation for displacement \hat{d} can be written as:

$$\hat{d} = argmin_{d \in \Omega} (E_1(d) + \alpha E_2(d)) \quad (2.3)$$

Equation 2.3 minimizes the energy of the cost function to estimate displacement \hat{d} . The cost function is constrained by two components: conservation (E_1) and regularization (αE_2), where α is a positive regularization coefficient. E_1 assumes that the echo amplitude is conserved during deformation (minimal decorrelation). The regularization term stabilizes the solution by minimizing local displacement variations [17]. Displacement estimates are found by minimizing the total energy, with coefficient α weighting the relative contributions of E_1 and E_2 .

There are three key parameters that can be adjusted to apply the ROF strain algorithm to clinical data: the regularization coefficient α , the search window size, and the numbers of spatial scales over which RF echo data are compared.

The search window size depends on the percent tissue compression that occurs between adjacent RF frames recordings. A search window that is too small may render the algorithm unable to find the global energy minimum. A search window that is too big may increase computation time as well as noise, which adds to the estimation uncertainty.

ROF employs a multi-scale approach to displacement estimation optimize the convergence of solutions while avoiding local minima. At each scale level $0 \leq i \leq I$, the image grid is partitioned into N_i equal sized data kernels [18] where N stands for the number of data kernels, and equation 2.3 is estimated. The highest scale level (coarsest) estimation is not constrained by the regularization term, thus allowing an initial global minimum to be found. This initial level is similar to that of the global companding process in the companding algorithm. At the lowest scale level (finest), the data kernel size is 4×1 pixels, which corresponds to the ratio of axial and lateral dimensions [18]. The number of iterations required for the solution to converge increases dramatically as the scale becomes finer. By changing the number of scale levels, both the computation and convergence time will be affected [17].

In actual C code, the program begins with the first level (maximum level with no regularization) search, the image grid is searched through a rough displacement map is obtained. This map is then written into blocks that is the size of the data kernel for the next search level. For all of the following search levels, the regularization term of equation 2.3 is also applied. After finding the minimum energy for each data kernel, the displacement map is updated and the data kernel size is halved for the following search level (Figure 2.3). This process is repeated until all of the search levels (as designated by the user) are finished.

Displacement and Strain

The C programming for the ROF algorithm directly produces the estimated displacement maps for the axial and lateral directions. Only the axial direction displacement map is used in the calculation of strain.

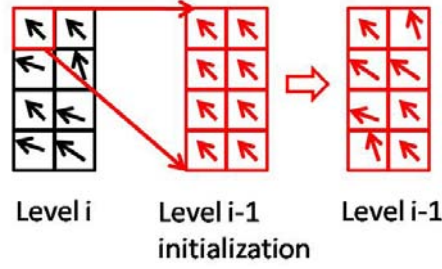


Figure 2.3: ROF Displacement Estimation. Starting at the top level (coarsest level) i , a rough displacement map is obtained for data kernels. In the next level, the smaller data kernels are initialized with displacement vectors obtained from the previous level. Minimum energy is then found and the displacement vectors updated. This process is repeated until the final size of the data kernel is 4×1 pixels.

A smoothing filter of 16 sample length is also used to smooth out the displacement map before strain is calculated. The strain is found by taking the derivative of the total displacement map.

2.2 Making the Phantom

All gelatin phantom specimens were constructed using 275 bloom strength, Type A, animal-hide gelatin powder provided by Fisher Scientific (Chicago, IL). To prepare the stiff center inclusion of the phantom, in a glass beaker, 100 ml of deionized water was combined with 13 ml of n-propanol and 10 g of gelatin powder to arrive at a 8% gelatin concentration. The solution is heated in a water bath at 60°C until visually clear (~ 35 min) and stirred every 15 minutes. The solution is then removed from heat and allowed to cool at room temperature ($21\text{-}22^\circ\text{C}$) until 50°C before adding 0.3 ml of formaldehyde. The solution is further cooled to 45°C and 9.1 g of graphite powder was added to act as the scattering particles for ultrasound. To prevent water loss, the beaker was covered with aluminum foil throughout the process. Finally, when the solution is cooled to 40°C and poured into a rigid, cylindrical container (diameter ≈ 1 cm), sealed, and placed on a slow rotator for 24 hours to prevent the graphic powders from settling. The stiff center inclusion is allowed to polymerize for 3 days before the rest of the phantom is made. To make the softer background phantom that surrounds the inclusion, the process is the same except that 6.75 g of gelatin powder was used to arrive at a 5.5% gelatin concentration. The inside of the 5 cm cubic container was sprayed with mold release and the stiff inclusion constructed earlier was inserted through the center of opposing sides of the acrylic mold as shown in Figure 2.4.

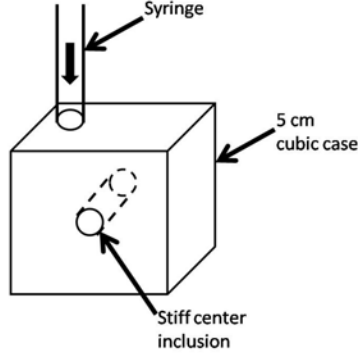


Figure 2.4: Schematic of the Mold Used for Creating Elasticity Imaging Gel Phantoms. A 4 inch C-clamp is used to hold the acrylic mold to the rotation table (not shown). A 10cc Leur-Lok syringe (with its tip removed) is positioned in the top of the mold for gel entry..

2.3 Imaging Techniques

The tissue-mimicking phantom was imaged with 2 separate Ultrasound systems: the Siemens Sonoline Antares ultrasound scanner with a VF10-5 linear array transducer and the Ultrasonix SonixRP ultrasound scanner (Ultrasonix Medical Corporation, CA) with a L14-5 linear array transducer. The Antares system was equipped with an Ultrasound Research Interface (URI) capable of recording radio-frequency (RF) echo data corresponding to the image displayed on the monitor for off-line processing. The SonixRP system was equipped with a C-compilable software package called Texo that allows for the automated process of recording RF echo data, however, the image cannot be displayed on the SonixRP monitor while the recording process is ongoing. Both scanners recorded data with frame rate of 4 frames per second and 17 frames per second. The RF frame rate was controlled through a waveform generator (Wavetek 30Ms/s Universal Waveform Generator Model 39) connected to the ECG trigger input of the Antares scanner or the trigger input of the SonixRP scanner. The waveform generator output a square wave signal with an amplitude of 50 mV peak-to-peak.

The compression process is done with a motion controller with feedbacks from a digital scale. The bottom surface of the phantom was coated in oil to simulate free-slip boundary conditions, and the top surface was coated with an acoustic coupling gel. The phantom was placed on the digital scale and a transducer holder with a flat acrylic plate was attached to the motion controller. The motion controller was programmed to ramp up to the applied stress level (between 850-900 Pa) in 1 second and was held constant for approximately 2000 seconds. A uniaxial stress was applied in the direction of the sound beam and normal to the top surface of the phantom via the acrylic plate. The digital scale provided stress measurement feedbacks to the motion controller in order to maintain the appropriate displacement to maintain constant stress. The RF echoes

were recorded at a depth of 1.5 to 4 cm.

2.4 Processing the RF Data

Strain images were estimated from the RF echo data collected from both ultrasound systems. RF data were collected from the tissue-mimicking gelatin phantoms. The data were processed both with a companding program based on the SAD algorithm and an optical flow algorithm. The echo data recorded at 4 frames per second were processed by the SAD companding program and the echo data recorded at 17 frames per second were processed by the regularized optical flow algorithm.

2.4.1 RF Data From 2 Systems

Both the Antares and the SonixRP ultrasound systems are programmed to record RF echo signals. However, due to the hardware differences between the two systems, the RF echo signals that were acquired were also slightly different from each other. For comparison purposes, the B-mode images, which are made from the envelope of the RF echo signals, are shown in Figure 2.5. Even though the stiffness of the center inclusion of the phantom is higher than the rest of the phantom, the amount of scatterers are the same throughout. Since the contrast from B-mode images depends on the intensity of the RF echo signals, we don't expect much contrast for these B-mode images. The approximate positions (not size) of the center inclusion are selected with black circles. Another thing to notice here is that the noise speckles in Figure 2.5b are much larger than that in Figure 2.5a. This is also due a hardware limitation of the SonixRP system which will be talked about later. Signal-to-noise ratio (SNR) calculations are conducted on both RF echo signals using equation 2.4, where net signal is determined by $signal = \mu_{signal} - \mu_{background}$ and RMS Noise is defined as the square root of the sum of variances from the signal region. The SNR calculated from the Antares RF data is 0.0358 and the SNR calculated from the SonixRP RF data is 0.0024. The RF signal acquired from the Antares ultrasound machine formed a better B-mode image with a better SNR value.

$$SNR = 20\log_{10} \frac{netsignal}{RMSnoise} \quad (2.4)$$

2.4.2 Processing of 4 Frames per Second RF Data

Both the Antares ultrasound system and the SonixRP ultrasound system were used to collect RF data with a rate of 4 frames per second. Upon initial processing, we obtain the following results in Figure 2.6.

From the strain images we can see that the strain estimated from the data from the SonixRP system is

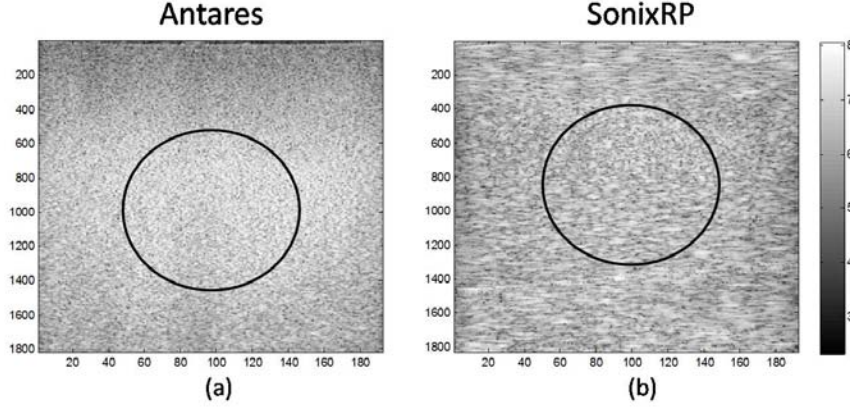


Figure 2.5: Antares and SonixRP B-mode Images. The black circles depict the approximate top position (not size) of the stiff inclusion. (a) B-mode image formed from RF echo data collected from Siemens Sonoline Antares system. (b) B-mode image formed from RF echo data collected from Ultrasonix SonixRP system.

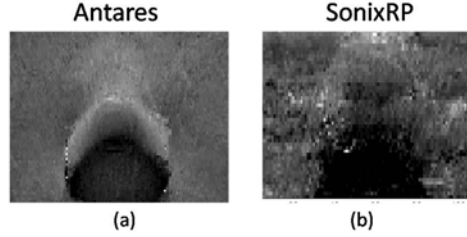


Figure 2.6: Antares and SonixRP before Adjustments Strain Images. The data was collected at a depth of 1 to 3.5 cm, therefore only the top half of the center stiff inclusion is shown (a) Strain Image obtained from RF data collected with the Antares ultrasound system at a sampling frequency of 40 MHz and lateral resolution of 200 μm ; (b) Strain Image obtained from RF data collected with the SonixRP ultrasound system at a sampling frequency of 20 MHz and lateral resolution of 300 μm .

less fine than the strain estimated from the data from the Antares system. By comparing the data collection parameters, we realized that there are several discrepancies between the Antares and the SonixRP ultrasound system:

1. The default axial sampling frequency of the SonixRP system (20 MHz) is half of that of the Antares system (40 MHz). This resulted in a worsening of the axial resolution of the data collected from the SonixRP system, and thus small displacements in the axial direction may not be recorded, resulting in a quantization error of the displacement map and a more blurry strain image.
2. The SonixRP L14-5 probe is has 128 physical elements, half of the number of physical elements in the Antares VF10-5 probe. The number of scanlines are also different, the SonixRP system produced B-mode images with a default of 128 scanlines (lateral resolution 300 μm), while the Antares system produced B-mode images with a default of 192 scanlines (lateral resolution 200 μm). This difference

in lateral resolution also results in a less detailed strain image.

The SonixRP system therefore had to be adjusted to sample the data at 40 MHz in the axial direction, and the number of scanlines changed by changing the activation of the virtual elements through the programmable Texo interface of the SonixRP system (please see Appendix for details). After adjustments, we were able to obtain the following strain images in Figure 2.7.

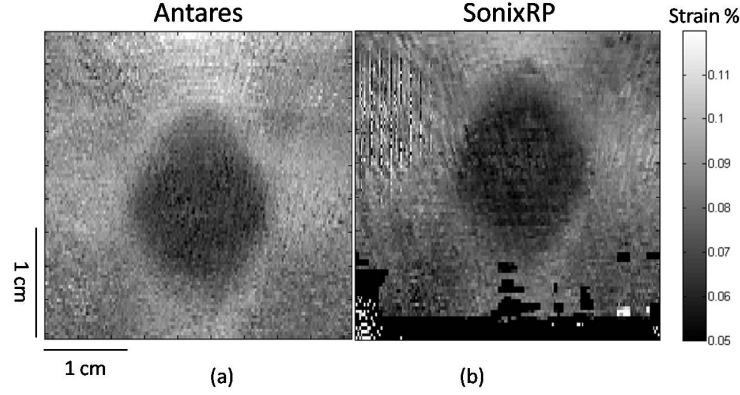


Figure 2.7: Antares and SonixRP after Adjustments Strain Images. The data was collected at a depth of 1.5 to 4 cm, the entire stiff center inclusion is shown (a) Strain Image obtained from RF data collected with the Antares ultrasound system at a sampling frequency of 40 MHz and lateral resolution of 200 μm ; (b) Strain Image obtained from RF data collected with the SonixRP ultrasound system at a sampling frequency of 40 MHz and lateral resolution of 200 μm .

From this we can see that the strain images now closely resemble each other near the center of the image but the bottom of Figure 2.7b appear decorrelated (black and white pixels). Since the main reason that we do strain imaging is to increase the contrast between non-homogenous regions in the tissue, we can compare between the contrasts in the strain images obtained from these two different ultrasound systems. Using equation 2.5 for contrast resolution (CR), where S_a is the signal inside of the stiff center inclusion and S_b is the signal in the background, we obtain $CR_{antares} = -0.13712$ and $CR_{sonixrp} = -0.11277$. This shows that the strain image obtained from the Antares RF echo data is approximately 17% better the strain image obtained from the SonixRP RF echo data.

$$CR = \frac{S_a - S_b}{S_a + S_b} \quad (2.5)$$

2.4.3 Processing of 17 Frames per Second RF Data

The 17 frames per second RF data were initially processed by the optical flow algorithm and the resultant strain image is shown in Figure 2.8.

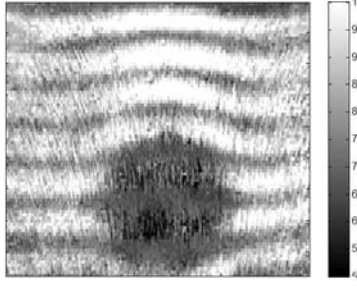


Figure 2.8: Antares 17 FPS Strain Image before Adjustments. The image contained quantization errors that presented as horizontal wave lines that distorted the image.

As we can see, the strain image is disrupted by horizontal wave lines. This is due to the quantization errors during the estimation of the displacement map. To explain this, we first investigate the search process for the SAD companding program. As mentioned previously in Section 2, the companding program works by matching a data kernel from image U with a data kernel in image C within a search region. After matching, the program produces a set of coordinates for the new position of the data kernel within the image grid. Since the search moves in units of pixels, any subpixel movement is disregarded. In other words, if a data kernel in U happens to have moved to a position that is in between two pixels, the resulting new coordinates are from a local minimum of equation 2.1 and not the global minimum. This is especially evident when the percentage of compression between adjacent RF frames is small. This is a different type of quantization error than the one resulting from a lowering of the sampling frequency of the ultrasound scanner as described previously.

Because of this limit in the search resolution (resolution = 1 pixel), the displacement map is presented as a series of staircase-shaped, linearly increasing lines instead of smooth lines. As seen in Figure 2.9a, the displacement estimation for a single scanline in the image matrix is plotted. Even though a smoothing filter is applied later on, the original map has lost much of the subpixel displacement, thus resulting in large spikes in the strain estimation as seen in Figure 2.9b.

A way to fix this is to use interpolation to restore the movements in between the steps in the staircases patterns. Since we know that displacement increases linearly within a small distance. We can use a linear interpolation method to estimate these subpixel displacements. For this interpolation, we assumed that the resolution is 0.2 pixels, and we obtain the following companded displacement and strain plots in Figure 2.10

This process can be run for the entire image matrix, and the before and after correction companded-only strain image is shown in Figure 2.11

The optical flow algorithm, which is used to estimate strain from RF data with a high frame rate (therefore percentage of strain between adjacent frame is small) suffers from the same problem (see Figure 2.8). When

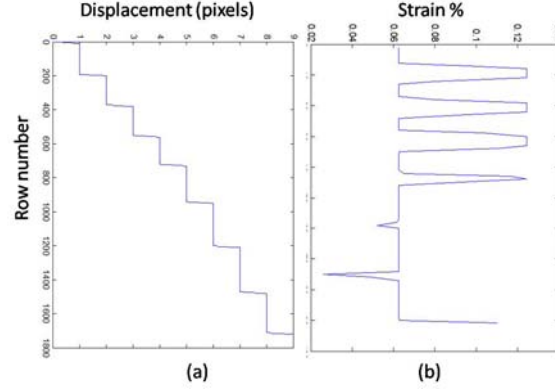


Figure 2.9: Displacement and Strain Plots for a Single Scanline with Quantization Error in the Image Matrix. (a) Displacement Plot. The large staircase patterns is a result of the search quantization error, due to the rounding of coordinates to whole integers, subpixel movements are disregarded; (b) Strain Plot. The quantization error is amplified when taking the derivative of the displacement plot to find strain. The large spikes are the horizontal wave lines seen in Figure 2.8.

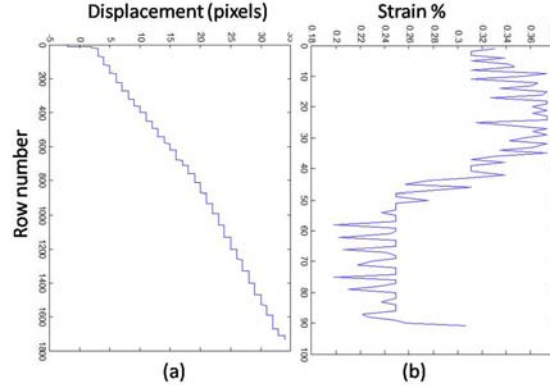


Figure 2.10: Companded Displacement and Strain Plots for a Single Scanline with Corrections for Companding in the Image Matrix. (a) Displacement Plot. The large staircase patterns is now interpolated to assume a resolution of 0.2 pixels; (b) Strain Plot. Without the large spikes in Figure 2.9, the true shape of the strain curve emerges.

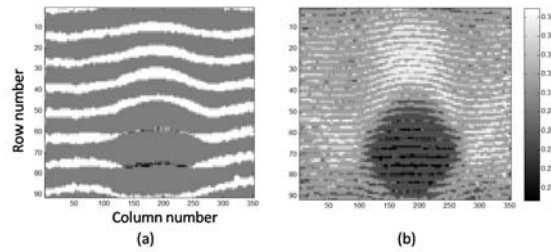


Figure 2.11: Companded-Only Strain Image before and after Corrections. (a) Companded-only strain image before correction, notice the horizontal wave lines that disrupts the image; (b) Companded-only strain image after correction, the actual strain image details are shown.

plotting out the displacement for a single scanline as estimated by the optical flow algorithm, we obtain Figure 2.12a.

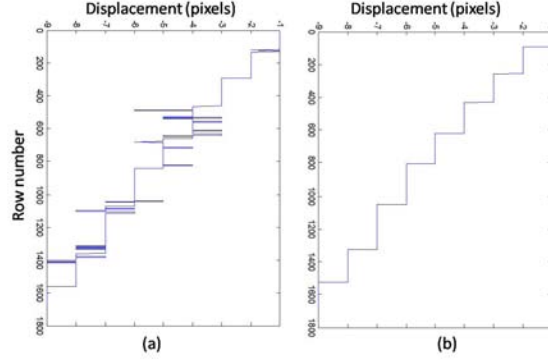


Figure 2.12: ROF Displacement Plots for a Single Scanline with Errors in the Image Matrix. (a) Displacement Plot before any corrections. The large staircase patterns is present, as well as many outliers; (b) Displacement Plot after a smoothing correction for the outliers.

A smoothing filter with a window length of 70 pixels was applied to the curve seen in Figure 2.12a. The idea is to filter out the outlier spikes using the "mode" function in Matlab. The corrected displacement curve is shown in Figure 2.12b.

After obtaining a clean displacement curve, the same interpolation method is applied, and the resultant displacement and strain curves are shown in Figure 2.13. After the entire image matrix is corrected, we obtain the following strain image (Figure 2.14). One thing we should notice is that the image appears smoothed out. This is a result of the smoothing filter (window length = 70 pixel) that is necessary to filter out the noises in the displacement staircase-like plots. A shorter smoothing filter (window length < 70 pixels) would not be sufficient in removing the displacement noises, which would then affect the interpolation step that is necessary in removing the quantization errors observed in Figure 2.8.

The same procedure was then applied to the 17fps RF echo data acquired by the SonixRP ultrasound system. The displacement and strain curves are shown in Figure 2.15. As we can see from the displacement plots, the bottom of the displacement plots showed big fluctuations in the estimation of the displacement vectors which were not present in the estimations from the RF echo data obtained from the Antares system. Since the SonixRP system was programmed to have its beam properties (e.g. lateral resolution, axial resolution) match the Antares system as closely as possible and both sets of RF echo data were processed by the same algorithm, plus the fact that the strain image estimated from the SonixRP RF echo data acquired at 4fps also showed decorrelation towards the bottom of the image, the only possibility that remains is that the quality of the signal as recorded by the SonixRP degrades towards the bottom of the image (farthest from the transducer probe surface). It is possible that the SNR towards the bottom of the image is too

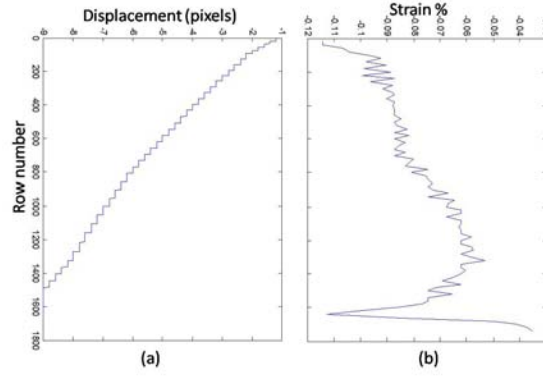


Figure 2.13: ROF Displacement and Strain Plots for a Single Scanline with Corrections for ROF in the Image Matrix. (a) Displacement Plot. The large staircase patterns is now interpolated to assume a resolution of 0.2 pixels; (b) Strain Plot.

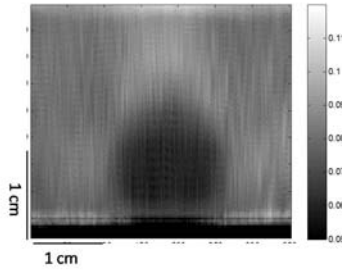


Figure 2.14: Antares 17 FPS Strain Image After adjustments. The horizontal wave lines are gone, however, the image appears more smoothed out.

low that random noises dominated the signal, which made it impossible for either algorithms to make a reasonable match between the data kernels of adjacent frames. Since the filtering/smoothing windows and the interpolation steps afterwards all depended on a fairly clean displacement estimation, the resulting strain image (shown in Figure 2.16) showed a loss in spatial resolution (image appear much smoothed out) as well as a decorrelated region at the bottom of the image.

Since most of the lesion is still visible, however, we can attempt to calculate the image contrast using equation 2.5 like before. We obtain $CR_{antares} = -0.14292$ and $CR_{sonixrp} = -0.12097$. This shows that, even with the decreased axial spatial resolution, the strain image obtained from the Antares RF echo data is approximately 18% better the strain image obtained from the SonixRP RF echo data.

2.4.4 Viscoelasticity Imaging

After the initial compression, the motion controller holds the compression plate and the transducer probe in place for an additional 30 minutes. The RF data acquired during this time records any possible viscoelastic

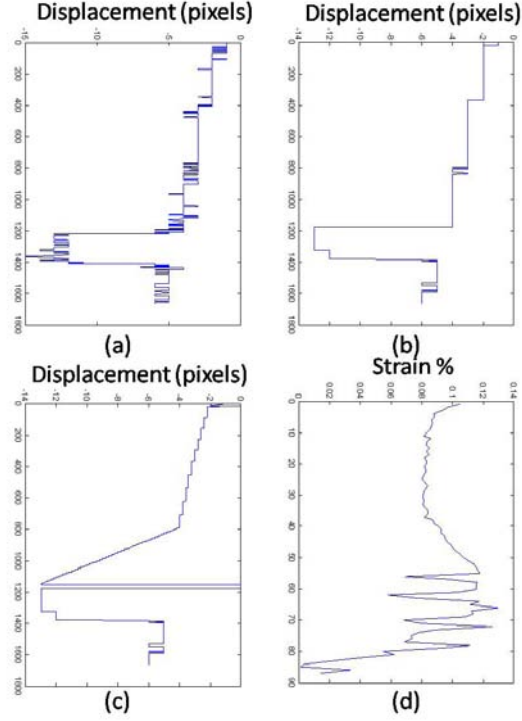


Figure 2.15: ROF Displacement and Strain Plots for a Single Scanline in the Image Matrix. The bottom of the displacement plots show vastly different displacement estimations that resulted in large spikes in the strain plot which in turn resulted in a decorrelated strain image for that region. (a) Displacement Plot with many noise. (b) Displacement Plot after noise corrections. (c) Displacement Plot with interpolation. The large staircase patterns is now interpolated to assume a resolution of 0.2 pixels; (b) Strain Plot.

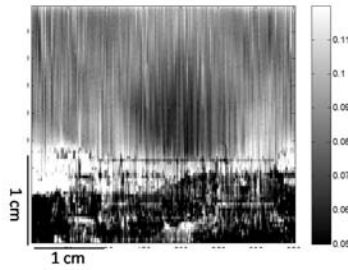


Figure 2.16: SonixRP 17 FPS Strain Image after Adjustments. The horizontal wave lines are gone, however, we lost spatial resolution and gained much decorrelated noises near the bottom of the image.

responses that the phantom may have. To produce the time-series of strain images needed for viscoelastic curve fitting, only simple correlation between adjacent images should be used since there are very little change between the corresponding RF signals from adjacent RF images. If companding is used between simple correlation, it may actually overcompensate and distort the RF signals.

2.5 Conclusions

Two different algorithms are used to produce the strain images from RF echo data (of frame rates 4 and 17 fps) recorded by two different ultrasound systems, the SonixRP ultrasound system (Ultrasonix Medical Corporation, CA) and the Siemens Sonoline Antares system. The advantage of the SonixRP system is the ability to program most transmit and receive aperture features, as well as the temporal pulse profile. However, hardware limitations on the SonixRP scanner made it necessary to program adjustments to its beamforming properties before obtaining strain images that can be compared to the Antares system.

The first major difference is the native (what the machine defaults to) sampling frequencies of the scanners. The SonixRP scanner has only half the sampling frequency as the Antares scanner. This means that only axial displacements that were twice as big as what was previously detectable on the Antares would be recorded on the RF echo data obtained from the SonixRP. This would be a major setback to the strain estimation algorithms since we are attempting to detect sub-pixel movements if possible. This difference in axial sampling frequencies can be changed through the programmable interface of SonixRP, so that both machines can now acquire RF echo data at 40 Mhz. The second major differences between the two systems is the linear array pitch. The number of physical elements on the SonixRP L14-5 linear array is only 128 while on the Antares VF10-5 linear array it is 256. Since the overall size of the transducer probes are similar, the result of less physical elements is that the pitch of the SonixRP linear array is about twice that of the Antares linear array. This presented a problem when we wanted to achieve a lateral resolution that is smaller than the pitch of the linear array, as we tried to do in the phantom study in order to make the RF image parameters between the two systems as similar as possible. The additional scanlines were interpolated in order to match up the lateral resolution of the two systems. As a result, the B-mode image obtained from the SonixRP scanner looked worse than the B-mode image obtained from the Antares scanner.

Even though both systems recorded the data at 16 bits. The SonixRP system works a little differently. As reported on the Ultrasonix Users Forum by the support engineer, the RF data is packed into 16 bits, but after the summation of 10 bit ADCs, the result will not be more than 14 or 15 bits. As tested by this engineer, he could obtain values up to 14 bits when the TGC gain is maximized. Since the SonixRP RF signals didn't actually have 16 bits worth of discrete values, the SonixRP RF signals are less detailed than the Antares RF signals and smaller displacements in the phantom may be missed.

From the strain image comparisons, we can see that the strain images produced by the SonixRP RF echo data is always a little worse in contrast than the strain images produced by the Antares RF echo data. Since patient studies required estimations of viscoelastic features which are obtained from a large collection of strain images, the Antares ultrasound system would be better suited for the study.

Chapter 3

Patient Imaging²

3.1 Methods

3.1.1 Patient Selection

Data were collected from 26 adult female patients through the breast clinic at UC Davis Medical Center in Sacramento, CA. Consent to participate was obtained from patients with a single, nonpalpable lesion identified by mammography just prior to undergoing a core needle biopsy procedure. The protocol was IRB approved at both UCD and UIUC. Data from 5 patients were rejected due to bad acquisition techniques that did not allow for further extractions of viscoelastic parameters needed for this study. Data from 21 patients were used for this clinical study. Out of these 21 patients, 10 patients were diagnosed with benign lesions and 11 patients with malignant lesions of various types. Patient ages ranged between 28 - 72 years, and tumor sizes ranged between 0.5-2.5 cm. The patients were selected randomly under the criteria that they have nonpalpable lesions that were identified via mammography. All lesions were BI-RADS 4 or 5, which identified these lesions as potentially malignant and requiring tissue diagnosis.

Biopsy samples from patients with malignant tumors were assigned SBR (Scarff-Bloom-Richardson) scores based on three morphologic features: degree of tumor tubule formation, tumor mitotic activity and nuclear pleomorphism of tumor cells. SBR scale assigns 1-3 points for each feature; the final score is the sum of all 3 (minimum 3, maximum 9) where higher scores indicate greater likelihood of tumor growth and metastasis. Tumors scoring between 3-5 are labeled Grade 1 (normal cell appearance); those with a score of 8 or 9 are labeled Grade 3 (poorly differentiated with tendency to grow and spread aggressively); and those with a score of 6 or 7 are in between. The SBR score and tumor grade aid physicians with treatment strategies and prognosis. Among the 11 patients with confirmed malignant tumors in our study, four were diagnosed as Grade 1 tumors, four as Grade 2, one as Grade 3, and 2 were not scored. Small size, low level of lymphatic invasion, low number of tumors per patient, lack of metastasis, and the tumor grades classify

²Portions of this chapter are reprinted from Y. Qiu, M. Sridhar, J. K. Tsou, K. K. Lindfors and M. F. Insana. Ultrasonic Viscoelasticity Imaging of Nonpalpable Breast Tumors: Preliminary Results. *Academic Radiology*, 15:1526-33, 2008. ©[2008 Elsevier]

our patient group as having early stage malignancies.

3.1.2 Lesion Diagnoses

Benign and malignant lesions were further classified into four subtypes or combinations with the exceptions of one benign lesion diagnosed as dense collagenous stroma and one malignant lesion diagnosed as B-cell lymphoma.

- a. *IDC*. Invasive/infiltrating ductal carcinoma (IDC) is the most common form of breast cancer, accounting for 65% to 80% of malignant mammary carcinomas [19]. Eight of 11 patients with malignant tumors were diagnosed with either IDC or IDC combined with DCIS (ductal carcinoma in-situ). All were Grade 1 or 2 and categorized as BI-RADS 4 or 5. While many IDC tumors have a stiff desmoplastic stroma surrounding the tumor, IDC tumors in our population were nonpalpable.
- b. *ILC*. Invasive lobular carcinoma (ILC) accounts for about 10% to 15% of all breast cancers [19]. Two of the 11 patients with malignant tumors were diagnosed with ILC. One had a Grade 1 tumor and both were classified BI-RADS 5. Both ILC patients were in their mid 50's to early 60's. Both had only one breast involved and no signs of metastasis. Early-stage ILC lesions are usually nonpalpable due to lack of desmoplasia reaction, difficult to observe mammographically, and thus often larger in size at diagnosis.
- c. *Fibroadenoma*. Seven of 10 patients with benign tumors were diagnosed with fibroadenoma. All of these patient images were categorized as BI-RADS 4.
- d. *Fibrocystic Change*. Two of 10 patients with benign tumors were diagnosed with fibrocystic changes. Both were BI-RADS 4 lesions. The condition is characterized by stiff noncancerous regions containing a high-density of normal ECM collagen and increased interstitial fluid pressure. However, our patient group presented no palpable lesions at physical examination.

All four lesion types usually express increased levels of ECM proteins, which tend to stiffen the lesion to varying degrees relative to their surround medium. IDC lesions with desmoplasia are particularly stiff, often palpable, and frequently they appear larger in the elastic strain image than on the sonogram [20]. By limiting our test population for VE imaging parameters to nonpalpable lesions, our study focuses on early disease that can be difficult to diagnose.

3.1.3 Imaging Techniques

Techniques for imaging viscoelastic features of breast tissues have been described previously [9, 21]. A Siemens Sonoline Antares ultrasound scanner was used with a VF10-5 linear array transducer operated at 8 MHz. The scanner was configured with an Ultrasound Research Interface (URI) capable of recording radio-frequency (RF) echo data corresponding to the image displayed on the monitor for off-line processing. Patients were positioned supine and the breasts were scanned anterior-posterior with the chest wall as compression support. Patients were instructed to hold their breath during the 12 to 15 seconds data acquisition time to minimize breast motion. The RF acquisition frame rate was 17 fps. Scanning was repeated at least three times for each patient to ensure consistency in the compressive motion of the breasts.

A small compressive force was applied manually to the breast surface by operators holding the transducer probe without restraint, the same as in clinical imaging. The operators apply a constant downward (compressive) force of approximately 4 N for the duration of the scan. Sridhar [9] showed that sonographers with limited training were able to keep the force constant within ± 0.24 N. The recording of RF echo frames began just prior to compression. The entire force was applied within 1 s and held constant while RF frames were recorded for 12 to 15 s. Echoes were recorded at an average depth of 30 mm.

3.1.4 Curve Fitting

From the time series of RF frames recorded during the application of the force, strain images were formed using multicompression techniques [22] and a regularized optical flow algorithm [17]. Figure 3.1 illustrates how we analyze the RF echo frames (totaling K frames) recorded over time by applying a sliding reference frame to form a time series of $K-1$ strain images. The k -th strain image in the series is made from adjacent RF echo frame pairs, f_k and f_{k+1} where $k=1, 2, 3, \dots, K-1$. Each strain image is spatially registered to match the geometry of the pre-compression sonogram. Strain is plotted over the time series of images to generate the viscous creep curve as shown in the figure. The VE phase of the curve begins immediately after tissue compression at time t_0 . One curve is computed for each strain pixel, or small group of pixels, from which VE parameters are estimated as described below.

VE parameters were extracted from each measured creep curve by least-square fitting of the patient data to a rheological model [23]. Our clinical imaging acquisitions are no longer than 15 s. Consequently the long-duration VE response terms are not engaged, and therefore a first-order discrete Kelvin-Voigt rheological model [9, 23] is appropriate,

$$\epsilon(t) = \epsilon_0 + \epsilon_1 \times \left(1 - \exp \frac{-t}{T_1}\right) \quad (3.1)$$

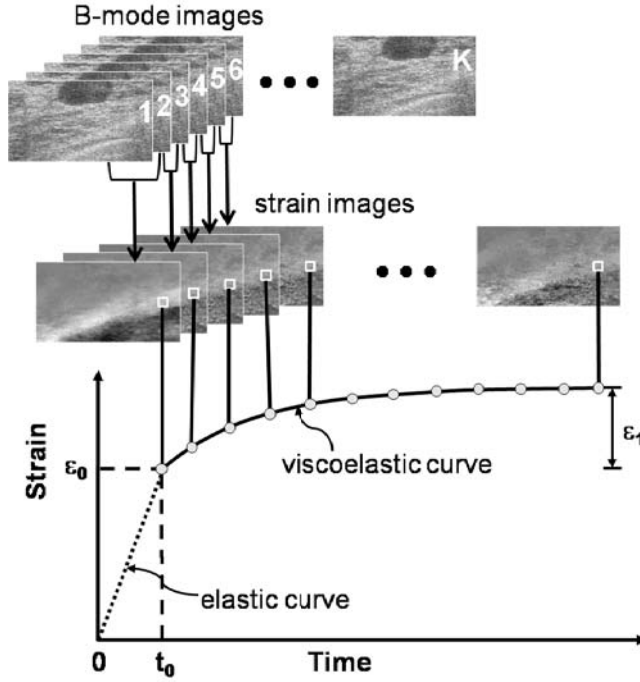


Figure 3.1: Multicompression RF Echo Acquisition, Strain Image Formation, and VE Parameter Estimation for a Patient with a Nonpalpable Fibroadenoma. ϵ_0 describes the instantaneous elastic strain. ϵ_1 describes the viscoelastic strain amplitude. Compression is applied from time $t = 0$ until t_0 during which the instantaneous elastic strain is measured. t_0 is also the time at which computation of the viscoelastic response begins. The viscoelastic curve lasts 12 to 15 seconds.

The term ϵ_0 is the instantaneous elastic strain that occurs immediately after compression (Fig 3.1). In the second term, ϵ_1 is the amplitude of the exponential creep curve. The constant T_1 is the retardation time of the curve characterizing the delay in the full strain response. Strain delays in stroma are from frictional resistance due to movement of the ECM in viscous interstitial fluids [9]. Elastic strain ϵ_0 , viscoelastic strain amplitude ϵ_1 , and the strain retardance time constant T_1 are the VE features analyzed in our study. Examples of malignant and benign VE curves are shown in Figure 3.2.

3.1.5 Pixel Selection and Averaging

Small areas 10×30 pixels were selected by hand within the lesion and background regions of each patient image (Fig 3.3). In those regions, the average B-mode, ϵ_0 , ϵ_1 and T_1 values from the spatially registered

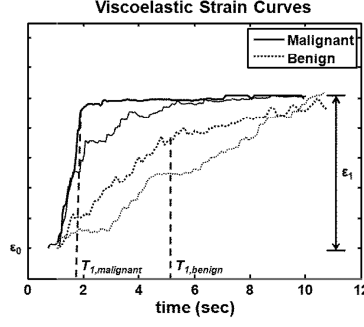


Figure 3.2: Examples of Malignant and Benign Viscoelastic Strain Curves. ϵ_0 describes the instantaneous elastic strain. ϵ_1 describes the viscoelastic strain amplitude. The retardance time constant T_1 measures the time required for the VE curve to reach a plateau. T_1 value for the malignant tumor is shorter than that for the benign tumor.

images are estimated. In cases of tissue heterogeneity, the selection area was reduced to 10×15 pixels, but consistency of the mean parameter values was maintained by repeating the process for difference area selections. For each image set, there are at least 5 selections per image that yields values that are within 15-20% of each other. These selections are averaged to give the mean values reported.

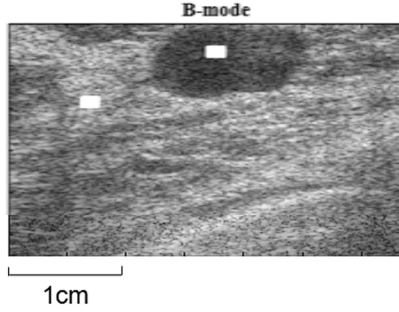


Figure 3.3: Example of Pixel Selection for Statistical Analysis. The selection boxes (marked in white) vary in size from 10×30 to 10×15 pixels.

3.1.6 Parametric Contrast

Contrast is an important visual feature for diagnosis, more than the parameters values. The goal of VE imaging is to provide tissue-specific parametric contrast for diagnosis. Contrast is calculated using

$$C = \frac{X_{lesion} - X_{background}}{\frac{X_{lesion} + X_{background}}{2}} = \frac{Difference}{Average} \quad (3.2)$$

where X_{lesion} and $X_{background}$ represents any of the four parameters described above from the lesion and background tissue areas of a patient scan.

3.1.7 The Three Adjustable ROF Parameters

As mentioned previously in the Phantom Imaging chapter, there are three adjustable parameters involved in the estimation of strain images from RF echo data using the Regularized Optical Flow algorithm: the regularization coefficient α , the search window size, and the numbers of spatial scales over which RF echo data are compared. These three parameters were varied to check for the differences in the visual appearance of the strain images, the computation time, and the resultant T_1 estimates. α is varied while the number of scale levels remained at 6 ($I = 5$) and the search window size remained at 8×2 pixels. The number of scale levels is then varied while α remained at 40 and the search window size remained at 8×2 pixels. Finally, the search window size is varied while α remained at 40 and the number of scale levels remained at 6.

Regularization Coefficient, α

Coefficient α was varied between 2 and 120 for a time series of strain images from the patient data set, and VE parameters were extracted for an infiltrating ductal carcinoma (IDC) lesion. α is proportional to the smoothness of the strain image; Figure 3.4a shows the resultant strain images when the coefficient is too small and Figure 3.4b shows a normal/smooth strain image. Strain noise suppression increases with α at the cost of spatial resolution. The recommended α value range of 2 to 10 [17] was unable to sufficiently minimize decorrelation noise, so we adopted a value of 40 for processing all patient data.

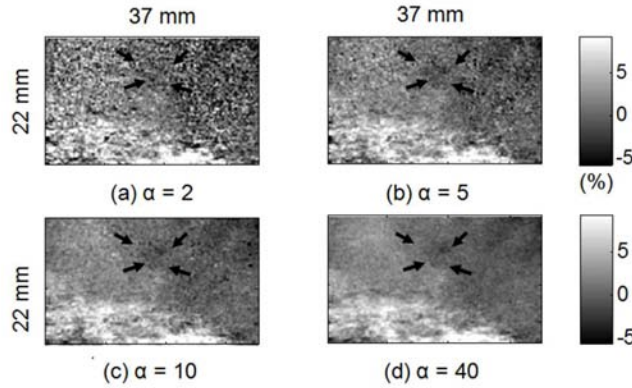


Figure 3.4: Strain Images with Different α . The lesion region is indicated with black arrows in (a) Strain image ϵ_0 when regularization coefficient $\alpha = 2$. Not enough noise suppression. (b) Strain image when $\alpha = 5$. There is some noise suppression. (c) Strain image when $\alpha = 10$. Minute noises still exist. (d) Strain image when $\alpha = 40$. The image is smooth.

T_1 values versus α are plotted in Figure 3.5 for a malignant lesion. T_1 values are stable for $\alpha \geq 40$ where much of the strain noise is suppressed. VE lesion contrast calculated in this range provided a reliable separation between benign and malignant lesions, thus improving diagnostic performance.

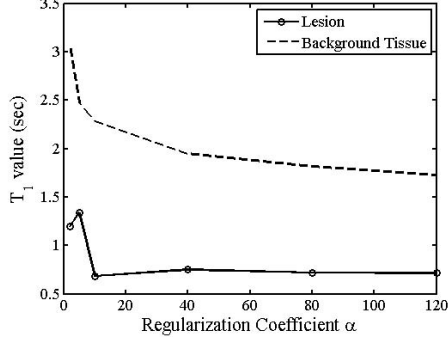


Figure 3.5: T_1 Estimates from the Lesion and Background Tissues Collected at Different α Values. Values below 40 shows bias in T_1 estimates because of strain noise, as shown in Figure 3.4.

Number of Scale Levels

The default number of scale levels as determined in [17] is $I = 5$ (6 levels). The anisotropic ratio of 4 is used to account for the ratio of axial-to-lateral block size. The number of scale levels used for our patient data was 6. The effect of the change on the computation time needed to process 166 strain images is shown in Table 3.1. Computational times for 7 scale levels are similar to those for 5 scale levels. However, strain images resulting from 5 scale levels failed to detect small parts of the breast tissue whereas the strain image resulted from 7 scale levels showed additional decorrelation noise. Therefore, the optimal number of scale levels for this study is 6.

Number of Scale Levels	ROF Computation Time (min)
5	69.2
6	80.8
7	91.3

Table 3.1: T_1 Computation Time for Different Number of Scale Levels

Search Window Size

The default search window size was 8×2 pixels (axial \times lateral). For comparison purposes, other search window sizes were used that were determined to be optimal for smaller and larger between-frame compression percentages in [17]. The resultant ROF computation time to process 166 strain images and the resultant T_1 contrast estimates are shown in Table 3.2. Although different search window size yielded similar T_1 contrast values ($T_1 = 0.8814 \pm 0.0066$), the computation time for the strain image sequence increases as the window size increases. A larger window size is ideal when there is a bigger change in the percentage strain between adjacent frames. For this patient study, a search window size of either 4×1 or 8×2 pixels is recommended due to the low percentage of strain between frames.

Search Window Time	ROF Computation Time (min)	T_1 Contrast
4×1	44.3	-0.8739
8×2	85.8	-0.8865
12×3	157.7	-0.8838

Table 3.2: T_1 Computation Time for Different Search Window Sizes

3.2 Results

3.2.1 Statistical Analysis

Average VE parameter values for the 21 patient studies are displayed in Figure 3.6 as histograms with error bars indicating standard errors. Due to the low number of patient studies in each lesion subtype, data were grouped into malignant and benign classes only. Two-sided t-tests were performed for each of the four parameters to test the hypothesis that data from the malignant and benign groups are really just one population. Parameters for which p values were less than 0.05 were considered able to distinguish between the two lesion groups. The t-tests results from data summarized in Figure 3.6 are shown in Table 3.3.

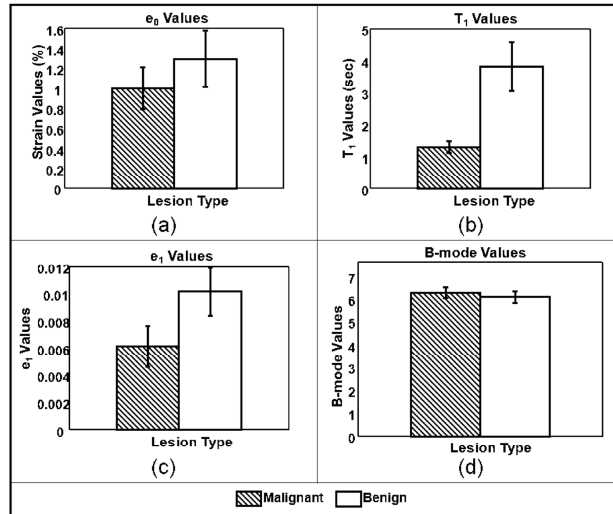


Figure 3.6: Average Lesion Parameters. (a) Elastic strain values ϵ_0 ($p < 0.5$); (b) Time constants T_1 ($p < 0.01$); (c) creep-curve amplitudes ϵ_1 ($p < 0.1$); and (d) B-mode pixel values ($p < 0.6$). Error bars denote ± 1 standard error.

Parameter	p -values (95% significance)
ϵ_0	0.4213
ϵ_1	0.0098
T_1	0.0986
B -Mode	0.5830

Table 3.3: Student's T-test Results from Viscoelastic Parameters

Only the VE retardance time constant, T_1 , was found to be separable and at the 99% significance level ($p < 0.01$). The histogram of Figure 3.6(b) shows the difference of means for T_1 clearly exceed the standard errors. For comparisons, we refer to the viscoelastic parameters found for normal glandular breast tissue from a previous study, $T_1 = 3.2 \pm 0.8$ s [9]. The current study summarized in Figure 3.6(b) shows an average T_1 value of 3.9 ± 0.7 s for benign tumors and 1.4 ± 0.2 s for malignant tumors. Therefore the difference in average T_1 values between normal parenchyma and malignant lesions is also highly significant. We also looked for correlations between T_1 image contrast, Eq 3.2, and tumor grade value (1-3), and we found the linear relationship $C_{T_1} = -0.18 \times \text{Grade} - 0.35$. The norm of the residuals for the equation fit was 0.014, suggesting strong correlation. However, there are too few samples to obtain the statistical power required for significance; therefore the result should be considered preliminary. Parameter uncertainties reported above are of the same order of magnitude as those caused by handheld force applicators. A previous study on normal volunteers [9] showed that the standard deviation for time constant estimates is typically 25% of the mean. Because the uncertainties are of the same magnitude on patients measurements, we infer that patient variability is small compared with operator variability.

3.2.2 Contrast Histograms and Scatter Plot

While the t-test for retardation time T_1 revealed a statistically significant difference between the mean values for benign and malignant tumors, it is important for image-based diagnosis to also explore contrast differences with respect to background areas. Equation 3.2 was applied to calculate patient contrast for each of the four parameters, B-mode, ϵ_0 , ϵ_1 , T_1 ; the results are shown in Figure 3.7, where we see that only T_1 provided statistically significant contrast.

Figure 3.8 shows a scatter plot of elastic strain (ϵ_0) contrast versus T_1 contrast for each of the 21 patients. In this figure, T_1 contrast is negative for all malignant tumors and positive for benign tumors, thus clearly providing lesion discrimination. None of the other features provided such strong discriminability.

3.2.3 Color Imaging

The previous section showed that spatially averaged T_1 contrast allows us to clearly discriminate nonpalpable malignant and benign breast lesions. This section explores spatial variations in the retardance time constant using color mapping of the T_1 contrast as an overlay on the sonogram. The concept is analogous to color-flow imaging where blood velocity is mapped onto the sonographic anatomy.

Consider each image as a matrix of size $I \times J$. For each pixel $p(i,j)$ in the matrix, $i = 1, \dots, I$ and $j = 1, \dots, J$, we compare its T_1 value to the spatially averaged T_1 value near the periphery of the image,

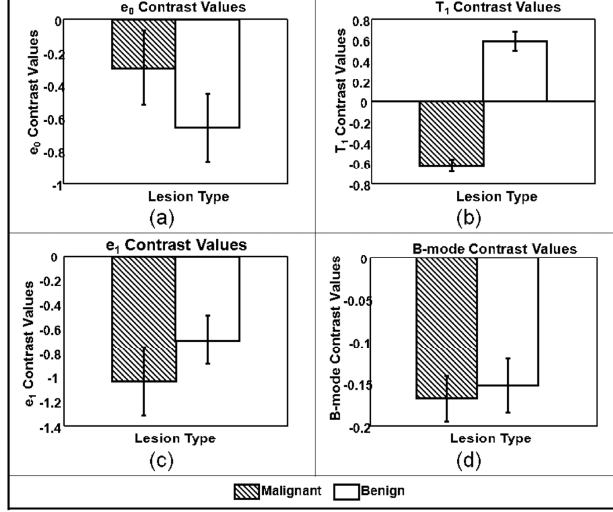


Figure 3.7: Patient Average VE Contrast Values for (a) elastic strain ϵ_0 , (b) T_1 , (c) ϵ_1 and (d) B-mode images. Error bars denote ± 1 standard error.

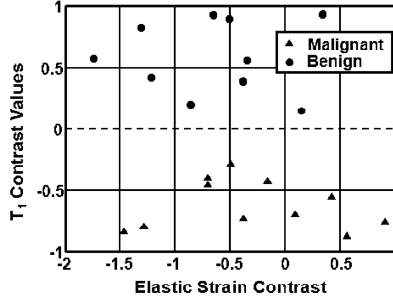


Figure 3.8: Scatter Plot of Patient Contrast Values for Two Parameters, ϵ_0 and T_1 . A dotted line drawn at T_1 contrast = 0 divides malignant and benign lesions. However, ϵ_0 contrast offers no significant discriminability.

$\overline{T_1}$ (selection box size 10×30 or 10×15 pixels). For pixels where $T_1(i,j) < \overline{T_1}$, we assign an overlay color in the blue spectrum where the shade indicates the negative difference value $T_1(i,j) - \overline{T_1}$. For pixels where $T_1(i,j) > \overline{T_1}$, we assign an overlay color in the red spectrum where the shade indicates the positive difference value $T_1(i,j) - \overline{T_1}$. For example, see the color bars in Figure 3.9 where an an isoechoic IDC lesion and a hypoechoic fibroadenoma are shown. These color pixels were spatially smoothed and amplitude thresholded in a manner similar to color-flow imaging.

3.3 Conclusions

This preliminary clinical study tentatively confirms the hypothesis that viscoelastic parameters from patients with nonpalpable breast lesions can be used to differentiate between malignant and benign breast tumors. A

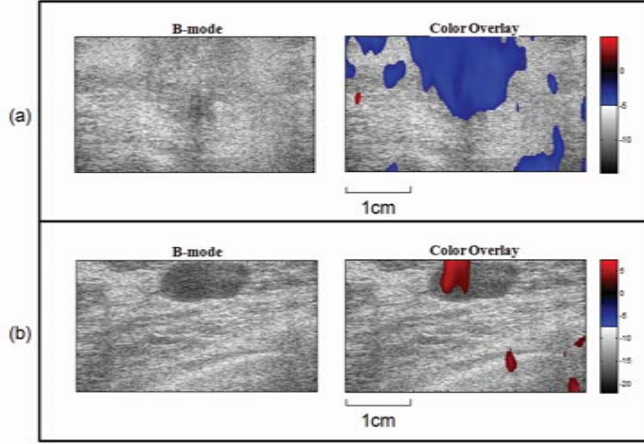


Figure 3.9: Sonograms with T_1 Parametric Color Overlays. The example in (a) is from a patient with a malignant (IDC) lesion; the negative T_1 contrast values are shown in blue. The example in (b) is from a patient with a benign (fibroadenoma) lesion; the positive T_1 contrast values are shown in red.

statistical test performed on four parameters, ϵ_0 , ϵ_1 , T_1 , B-mode, showed a significant difference between the retardation time constants T_1 for the two lesion types. In addition, T_1 contrast was found to be negative for malignant lesions and positive for benign lesions in all 21 patient studies. The observed contrast differences are consistent with known changes in the collagenous stromal ECM near the lesion [24]. Benign tumors have increased normal collagen density; that is, the associated proteoglycan content increases in proportion. Dense ECM increases both the cross linking among collagen fibers and the viscosity of interstitial fluids, which increase the resistance to creep and lengthen T_1 values. Very similar results were found in VE phantom studies where hydropolymers density was locally increased [23]. Malignant tumors also have increased collagen density; however these collagen fibers are structurally different from those of normal ECM stroma. Malignant stroma has reduced proteoglycan content for loose and dense connective breast tissues that then reduces the frictional forces resisting creep. Consequently, T_1 values in nonpalpable lesions are less than with that of normal breast stroma. In other words, IDC and ILC lesions are generally more fluidic in their mechanical response than the more solid-responding fibroadenomas. We point out that lesion palpability is determined very subjectively. A study with more patients is required to reach conclusion about clinical efficacy.

As we discovered previously by comparing VE results from breast tissues of normal volunteers [9] and hydropolymers phantoms [23] over much longer acquisition times (200 s and 3600 s, respectively), the RF acquisition time significantly influences lesion contrast. Eigenanalysis of normal breast tissues [9] suggests there are at least two VE components in the rheological model for 200 s breast acquisitions using our quasi-

static elasticity imaging method. The VE retardance time constants are $T_1 = 3.2 \pm 0.8$ s and $T_2 = 42 \pm 28$ s. By truncating the acquisition time to practical values < 20 s, as in the current study, we can ignore the effects of T_2 on T_1 , and we can expect a coefficient of variation for T_1 estimates of 25% due mostly to jitter from the hand-held force application [9]. The current study did not examine the T_2 component because 200 s acquisitions were impractical. Also there is greater relative error for T_2 estimates, which is a tissue response at a much lower force bandwidth (< 0.1 Hz) and which requires development of new scanning techniques. Nevertheless, we are encouraged by the diagnostic performance of T_1 estimates for malignant-benign discrimination.

Potential sources of error in viscoelasticity imaging are patient movement (respiratory and cardiac) and hand-held transducer movement during force application. Small transducer movements increase decorrelation errors in strain images [22, 17], which then propagate into large noise variations in VE parametric images. Changing to the high-frequency force stimuli used in dynamic imaging methods [4, 5, 6, 7] reduces VE parameter estimation errors for several reasons. However, we know from the polymer mechanics literature that the frequency of the applied force influences the time-varying strain response and therefore VE parameters. To visualize this point, consider movement of stroma: an ECM polymer embedded within a viscous interstitial fluid. Slow application of a compressive force allows fluid motion with little frictional resistance, and therefore cross linking among ECM fibers determines the VE response. However, dynamic friction increases with the velocity of the applied force, depending on the viscosity of the fluid, until fluid flow dominates the time-varying strain response. Consequently, there is merit in pursuing both quasi-static and dynamic elasticity imaging methods. Both methods are currently limited for clinical applications by our ability to precisely apply forces to the tissue.

Results from this preliminary study have demonstrated that viscoelastic imaging of breast tumors can effectively aid in the characterization of nonpalpable breast lesions. The greatest advantage of this novel imaging method is that the viscoelastic parameters obtained can be used to clearly differentiate between malignant and benign lesions for patients with nonpalpable, early stage, BI-RADS 4 and 5 breast tumors. The addition of viscoelastic features into the diagnosis feature space can aid the physicians in making a more accurate diagnosis of early breast cancer patients.

Chapter 4

Conclusions

The emergence of accurate diagnostic tools for the detection of early, non-palpable, suspicious breast lesions is very important in improving the overall survival rate of the cancer patients. Women who come in for their annual breast exams may have small lumps (<2 cm) in their breasts that are not detectable via manual palpation but appear suspicious on medical imaging devices such as ultrasound (breast sonogram) and x-ray (breast mammogram). The next logical step would be a core-needle or fine-needle aspiration biopsy to obtain tissue samples for examination by the pathologists. The biopsy result would establish the type, stage of the tumor as well as any possible nodal involvement and metastasis. However, biopsies count as minor surgeries which would carry risks of infections and up to half of these biopsies can turn out to be unnecessary as the lesions are benign. The ideal situation then would be to develop a non-surgical technique that would help to eliminate some of the unnecessary biopsies and provide more information than simple detection of breast lesions.

In the preliminary patient studies we used ultrasound elastography techniques to study the viscoelastic responses of non-palpable breast lesions. An ultrasound probe is used to apply and hold the compression to the breast region where a small, non-palpable, suspicious lesion is present and record the displacement of the tissue over time (~ 17 seconds). Strain images are calculated from displacement maps which are estimated by correlation algorithms using the time-series of RF echo data recorded. Viscoelastic information are then extracted from the time-series of strain images through curve-fitting. Because of the many estimations (where errors from the previous estimation are amplified in the next) we have to go through in order to extract information that may be useful in distinguishing between malignant and benign breast lesions, it is very important to have a good set of RF echo data to begin with. And since we are dealing with lesions of very small diameters (<2 cm), we would want the spatial resolution to be high so that the viscoelastic parameters obtained are useful for further diagnosis. The phantom study compared strain images of the same tissue-mimicking phantom estimated by the same correlation algorithms using RF echo data recorded from two different ultrasound systems. The Ultrasonix Sonix RP system produced strain images that had poorer spatial resolution and contrast than the Siemens Sonoline Antares system. If we are to estimate

viscoelastic parameters from these strain images, the results may be a false-positive diagnosis for the patient because the viscoelastic parameter values may not be accurate. Therefore, an ultrasound machine with high spatial resolution would be better in ultrasound viscoelasticity studies.

Using the RF echo data that we have acquired using the Antares ultrasound machine, we were able to conduct a preliminary study that yielded some interesting results. The ability of the viscoelastic parameter T_1 in discriminating between malignant and benign lesions can be a very useful addition to the diagnostic features of ultrasound. A larger study with more patient data may reveal more about the sensitivity and specificity of T_1 contrast discrimination of breast lesions, and may even provide further information on the specific types of breast lesions being studied. This noninvasive technique has the potential to reduce the number of unnecessary biopsies while providing the doctors and patients with some early diagnostic information on suspicious breast lesions.

Appendix A

SonixRP Adjustments

The Texo demo program is written in C code. Using this program, the SonixRP system produces 128 scanlines in the RF images by default, corresponding to the 128 physical elements available in the transducer array. The Texo demo C code divides each physical elements (numbered 0 to 127) into 10 virtual elements (numbered 0 to 9). and so there are 128×10 virtual elements that you can control. In order to change the number of scanlines in the RF image, we have to change which virtual elements are the center elements.

By default, every 5th virtual elements of every physical element is activated. In other words, if we let the current physical element number be i , then every $(i \times 10) + 5$ virtual element is designated the center element and a scanline is added at the position.

If we wish to increase the number of scanlines, thereby interpolating between elements, we need to change the designation of the center element. For 192 scanlines, the virtual elements are in a sequence as follows: 0, 6, 13, 20, 26, 33, 40, 46, 53, 60, 66, 73, 80, 86... Basically, every 6th or 7th virtual element is designated as the center element. To figure out how to assign this in the C code efficiently, it is helpful to draw a picture of the virtual elements like in Figure A.1. As we can see, the center virtual element position on the physical element repeats itself for every 2 physical element, since the position of the center virtual element on physical element $i+2$ is the same as the position of the center virtual element on physical element i , we can simplify the C code by assigning the right center virtual element positions to the even and odd numbered physical elements.

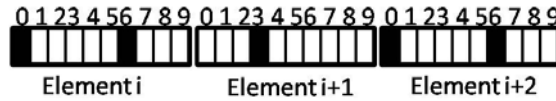


Figure A.1: Diagram for 192 Scanlines Center Virtual Element Assignment. The center virtual element is represented by a solid black rectangle. The center virtual element position on the physical element repeats itself for every 2 physical elements.

The same can be done for 360 scanlines, but the space between center virtual elements will be smaller. In this case, the spacing between the center virtual elements are 3 or 4 virtual elements, and it is harder to

find a pattern. It would be more useful to write out the designation for every single center virtual elements and then combine those that have the same line of code.

References

- [1] American Cancer Society. Cancer facts & figures 2007. Technical report, Atlanta: American Cancer Society, 2007.
- [2] M. F. Insana and S. A. Wickline. Multimodality biomolecular imaging. In *Proceedings of the IEEE*, volume 96, pages 378–381, 2008.
- [3] F. Moinfar, Y. G. Man, L. Arnould, G. L. Bratthauer, M. Ratscheck, and F. A. Tavassoli. Concurrent and independent genetic alterations in the stromal and epithelial cells of mammary carcinoma: Implications for tumorigenesis. *Cancer Research*, 60:2562–2566, 2000.
- [4] J. F. Greenleaf, M. Fatemi, and M. F. Insana. Selected methods for imaging elastic properties of biological tissues. *Annual Review of Biomedical Engineering*, 5:57–78, 2003.
- [5] R. Lerner and K. Parker. Sonoelasticity imaging. *Acoustical Imaging*, 17:317–327, 1988.
- [6] R. Sinkus, M. Tanter, T. Xydeas, S. Catheline, J. Bercoff, and M. Fink. Viscoelastic shear properties of in vivo breast lesions measured by mr elastography. *Magnetic Resonance Imaging*, 23:159–165, 2005.
- [7] M. Fatemi and J. F. Greenleaf. Ultrasound stimulated vibro-acoustic spectrography. *Science*, 280:82–85, 1998.
- [8] A. Sharma, M. Soo, G. Trahey, and K. Nightingale. Acoustic radiation force impulse imaging of in vivo breast masses. In *Proceedings of the IEEE Ultrasonics Symposium*, volume 1, pages 728–731, 2004.
- [9] M. Sridhar and M. F. Insana. Ultrasonic measurements of breast viscoelasticity. *Medical Physics*, 34:4757–4767, 2007.
- [10] A. Thomas, S. Kümmel, F. Fritzsche, M. Warm, B. Ebert, B. Hamm, and T. Fischer. Real-time sonoelastography performed in addition to b-mode ultrasound and mammography: Improved differentiation of breast lesions. *Academic Radiology*, 13:1496–1504, 2006.
- [11] A. Thomas, M. Warm, M. Hoopmann, F. Diekmann, and T. Fischer. Tissue doppler and strain imaging for evaluating tissue elasticity of breast lesions. *Academic Radiology*, 14:522–529, 2007.
- [12] H. Zhi, B. Ou, B. M. Lou, X. Feng, Y. L. Wen, and H. Y. Yang. Comparison of ultrasound elastography, mammography, and sonography in the diagnosis of solid breast lesions. *Journal of Ultrasound in Medicine*, 26:807–815, 2007.
- [13] A. Itoh, E. Ueno, E. Tohno, H. Kamma, H. Takahashi, T. Shiina, M. Yamakawa, and T. Matsumura. Breast disease: Clinical application of us elastography for diagnosis. *Radiology*, 239:341–350, 2006.
- [14] P. Chaturvedi, M. F. Insana, and T. J. Hall. 2-d companding for noise reduction in strain imaging. *Ultrasonics, Ferroelectrics, and Frequency Control, IEEE Transactions*, 45:179–191, 1998.
- [15] L. N. Bohs and G. E. Trahey. A novel method for angle independent ultrasonic imaging of blood flow and tissue motion. *Biomedical Engineering, IEEE Transactions*, 38:280–286, 1991.

- [16] L. N. Bohs, B. H. Friemel, B. A. McDermott, and G. E. Trahey. A real time system for quantifying and displaying twodimensional velocities using ultrasound. *Ultrasound in Medicine and Biology*, 38:280–286, 1994.
- [17] C. Pellot-Barakat, F. Frouin, and M. F. Insana. Ultrasound elastography based on multiscale estimations of regularized displacement fields. *Medical Imaging, IEEE Transactions*, 23:153–163, 2004.
- [18] C. Pellot-Barakat, F. Frouin, A. Herment, J. J. Mai, K. K. Lindfors, J. K. Tsou, P. Von Behren, and M. F. Insana. A regularized approach for freehand ultrasound elastography of breast lesions. In *Biomedical Imaging: Nano to Macro, IEEE International Symposium*, volume 1, pages 952–955, 2004.
- [19] P. P. Rosen. *Rosen’s Breast Pathology*. Lippincott Williams & Wilkins, Philadelphia, 2001.
- [20] B. S. Garra, E. I. Cespedes, J. Ophir, S. R. Spratt, R. A. Zuurbier, C. M. Magnant, and M. F. Pennanen. Elastography of breast lesions: Initial clinical results. *Radiology*, 202:79–86, 1997.
- [21] M. F. Insana, C. Pellot-Barakat, M. Sridhar, and K. Lindfors. Viscoelastic imaging of breast tumor microenvironment with ultrasound. *Journal of Mammary Gland Biology and Neoplasia*, 9:393–404, 2004.
- [22] H. Du, J. Liu, C. Barakat, and M. F. Insana. Optimizing multicompression approaches to breast elasticity imaging. *Ultrasonics, Ferroelectrics and Frequency Control, IEEE Transactions*, 53:90–99, 2006.
- [23] M. Sridhar, J. Liu, and M. F. Insana. Viscoelasticity imaging using ultrasound: Parameters and error analysis. *Physics in Medicine and Biology*, 52:2425–2443, 2007.
- [24] G. Losa and M. Alini. Sulphated proteoglycans in the extracellular matrix of human breast tissues with infiltrating carcinoma. *International Journal of Cancer*, 54:552–557, 1993.